PHYSICAL REVIEW MATERIALS **3**, 123602 (2019)

Misorientation-dependent solute enrichment at interfaces and its contribution to defect formation mechanisms during laser additive manufacturing of superalloys

Avinash Hariharan,[1,*] Lin Lu,[1] Jeroen Risse,[2,3] Aleksander Kostka,[4] Baptiste Gault,[1,5] Eric A. Jägle,[1] and Dierk Raabe[1]
[1]*Department of Microstructure Physics and Alloy Design, Max-Planck-Institut für Eisenforschung GmbH,*
Max-Planck-Straße 1, 40237 Düsseldorf, Germany
[2]*Fraunhofer-Institut für Lasertechnik ILT, Steinbachstraße 15, 52074 Aachen, Germany*
[3]*Advanced Research and Development Additive Manufacturing,*
TRUMPF Laser- und Systemtechnik GmbH, Campus Boulevard 79, 52074 Aachen, Germany
[4]*Center for Interface Dominated Materials (ZGH), Ruhr- University Bochum, 44801 Bochum, Germany*
[5]*Department of Materials, Royal School of Mines, Imperial College, London SW7 2AZ, England, United Kingdom*

(Received 11 August 2019; published 20 December 2019)

A vital issue during selective laser melting of nonweldable polycrystalline nickel-base superalloys is the formation of microcracks. These are cracks occurring during the last stage of solidification and only at high angle grain boundaries (HAGBs). Solute enrichment to the remaining interdendritic liquid and its partial back-diffusion into the solid contributes to the crack nucleation mechanism. Here we use atom probe tomography coupled with transmission Kikuchi diffraction to determine the misorientation and chemical composition profiles across HAGBs (with and without cracks) and across crack-free low angle grain boundaries (LAGBs). The Gibbsian interfacial excess of solutes (mainly B, C, Si, and Zr) is at least two times higher at the HAGB compared to the LAGB. The chemical profiles show the opposite behavior to established model predictions of the last stage of solidification. Our diffusion calculations elucidate that the chemical profiles are influenced by both microsegregation (of Ti, Nb, and Si) during solidification and solid-state segregation (of B, C, and Zr) during cooling. The chemical profiles in the topmost layer indicate a negligible effect of remelting and reheating. Except for Ti-rich carbides, no secondary phases are found. Additionally, we study an alloy with a reduced content of Zr and Si (by at least 60 wt. %), relative to the standard IN738LC composition. We achieved a 99% reduction in crack length per unit area. However, the grain boundary enrichment of Zr and Si in the modified alloy was similar to the standard alloy. Based on these findings, we critically discuss the contribution of various mechanisms proposed for solidification cracking.

DOI: 10.1103/PhysRevMaterials.3.123602

I. INTRODUCTION

Nickel-base superalloys (NBSs) have excellent high-temperature oxidation resistance and mechanical strength due to their two-phase microstructure consisting of γ phase matrix and γ' precipitates [1–4]. Hence, they are used in the land- and aircraft-based gas turbine components [5,6]. Due to the geometrical complexity of these components as well as repair opportunities, additive manufacturing of NBSs is of significant interest for the aerospace and power-generation industries [7]. Selective laser melting (SLM, also termed laser powder bed fusion) is a widely used powder bed additive manufacturing process being developed as an economically viable solution for processing NBSs [7]. In SLM, a digital three-dimensional (3D) model of the component is virtually sliced into multiple layers and a laser beam, focused onto the powder bed, then physically manufactures each layer. Currently, most NBSs used in SLM were originally developed for processing by casting with a polycrystalline microstructure. One example of such an alloy is Inconel-738LC (IN738LC).

The key issue in additive manufacturing of γ'-strengthened NBSs is the formation of cracks during the SLM process and the postprocessing [7–10]. The first type of cracks occurring during SLM is microcracks, also referred to as "hot cracks." The second type is strain-age cracks that can appear during heat treatment of the alloy subsequent to SLM. This type of cracking is outside the scope of the current paper.

Solidification cracking is a type of hot cracking that occurs in polycrystalline superalloys during casting and welding at the terminal stage of solidification [11–14]. Solidification cracks progress by rupturing of thin liquid films in the semisolid region. These liquid films are along the interdendritic regions that will eventually form grain boundaries (GBs) upon full solidification [14,15]. Earlier works on laser welding of cast γ/γ' IN738LC superalloy parts have revealed the material's susceptibility to the second type of hot cracking, known as heat affected zone (HAZ) cracking [5,16–18]. HAZ cracks, also called liquation cracks, result from the remelting of low-melting phases along grain boundaries such as γ/γ' eutectics, some MC-type carbides, and the γ' precipitates [5,6,16–20]. However, in as-SLM-produced samples, low-melting phases along grain boundaries are not present, and,

---

[*] Corresponding author: a.hariharan@mpie.de

TABLE I. Crack formation mechanisms in γ' strengthened nickel-base superalloy.

Crack type	Location of occurrence	Time of occurrence	Mechanism
Solidification crack	High angle grain boundaries, i.e., intragranular	Last stage of solidification	Decohesion of liquid films due to tensile stress
Liquation crack	High angle grain boundaries in the heat-affected zone, i.e., intragranular	Reheating due to the next laser pass	Decohesion of liquid low-melting phases at grain boundaries
Strain-age crack	Grain boundaries	During postheat treatment	Reduction in the local ductility

hence, hot cracking during SLM cannot be attributed to HAZ cracking [21,22]. A description of solidification and liquation and the strain-age cracking phenomenon is detailed in Table I.

Solidification cracking remains a fundamental problem in many alloys during casting, welding, and additive manufacturing due to the complex interplay between the thermomechanical and metallurgical factors involved [11,23]. Models for solidification cracking initially established for castings have been further extrapolated to welding conditions by accounting for the higher thermal gradients and cooling rates, however inheriting the limitations of the original models [24]. Earlier work on the mechanism of solidification cracking showed enrichment of alloying elements in the interdendritic liquid. This effect increases the liquidus-solidus temperature range, thus enhancing solidification cracking susceptibility [15,25,26]. However, studies on cracking in as-cast NBS variants showed an insignificant influence of the solidification range on the cracking susceptibility [27–30].

The onset of cracking is predominantly influenced by the solidification behavior of the alloy, at the last stage of solidification, when the fraction of the liquid phase, $<1\%$, is present at the interdendritic region [31–33]. At this stage, the interdendritic liquid forms either a continuous film of a few nanometers in thickness or a discontinuous set of droplets. The coalescence of this confined liquid depends on the solid-liquid interface energy (γ_{SL}) and the grain boundary energy (γ_{GB}) [34]. Wang *et al.* [34] showed experimentally that in attractive interfaces, which are essentially low angle grain boundaries (LAGBs) ($\gamma_{\mathrm{GB}} - 2\gamma_{\mathrm{SL}} < 0$), the solid-liquid film coalesces to a GB instantly. However, a liquid film present at a repulsive interface, which is a high angle grain boundary (HAGB) ($\gamma_{\mathrm{GB}} - 2\gamma_{\mathrm{SL}} > 0$), needs additional undercooling, $\Delta T_b(\theta)$, to solidify. This is given by the equation

$$\Delta T_b(\theta) = \frac{[\gamma_{\mathrm{GB}}(\theta) - 2\gamma_{\mathrm{SL}}\ ]\,T_m}{L\,\delta} \tag{1}$$

where θ is the misorientation angle (°), T_m is the melting temperature (K), L is the heat of fusion per unit volume ($\mathrm{J\,m^{-3}}$), and δ is the interface thickness (GB or solid-liquid interface in nanometers). Hence, solidification cracks are exclusively observed along HAGBs, the high γ_{GB} of which stabilizes the liquid film and leads to an additional undercooling required for full solidification [35]. The model by Rappaz *et al.* [35] describes this influence of the misorientation between grains adjacent to a liquid film on film stability and hence cracking propensity. The misorientation, and therefore the stability of the liquid film, influences the liquid phase composition [35,36]. The model predicts a different composition profile across grain boundaries (upon full solidification) depending on their misorientation.

The presence of grain boundary solidification cracks in SLM-processed IN738LC was initially reported by Rickenbacher *et al.* [21]. Further studies showed the effect of minor alloying elements on the cracking susceptibility [8,37]. Engeli *et al.* [37] report that a reduction in Si content in the alloy powder was beneficial for reducing the intergranular crack density. They hypothesize that Si enrichment at grain boundaries leads to the formation of detrimental phases and hence to cracking. However, they give no experimental support for the existence of such phases. Cloots *et al.* [8] observe intergranular solidification cracks on a grain boundary along the build direction (BD) of SLM-produced IN738LC. However, due to the small size of dendrites and, therefore, the extremely high density of low and high angle grain boundaries in SLM-produced alloys, the misorientation of the GB in their atom probe tomography (APT) analysis is ambiguous. Cloots *et al.* hypothesize that the increase in the liquidus-solidus interval due to Zr enrichment at the GB is responsible for solidification cracking. However, as mentioned previously, the solidification interval is not a reliable indicator for cracking behavior. Additionally, the enrichment of Si and its effect on the cracking mechanisms were not discussed in this study.

Minor alloying elements such as B and Zr are usually present in small amounts in NBSs. Earlier work [38,39] suggests that trace additions of B reduced the solidification interval and additions of Zr increased it. Holt and Wallace [38] showed that cracking susceptibility in NBS castings could be reduced by eliminating the Zr content. Zhang and Singer proposed as an alternative mechanism that the enrichment of Zr and B in the liquid could affect the surface tension of the liquid melt, thereby increasing grain boundary wettability [30]. This results in the nonuniform bridging of the coalescing arms of the growing dendrites, which promotes incomplete solidification and hence initiating cracks.

The effect of Si on the weld crack susceptibility of superalloys is contentious, and reports are contradictory. Studies show beneficial [40], neutral [41], and detrimental effects [37] in different superalloys. Hence, the influence of minor solute elements on the solidification behavior of superalloys remains under debate. This emphasizes the need to revisit the mechanism behind solidification cracking during SLM processing of nickel-base superalloys, with a focus on the effect of minor alloying elements and their distribution across grain boundaries.

It is acknowledged that the solidification cracking can only occur when the two necessary conditions, namely, the evolution of significant tensile stresses across the interfaces and the presence of an interdendritic liquid film, occur simultaneously. However, for SLM, tensile stresses evolve throughout the entire build during the process [42–45]. As a result, the microstructure of the SLM-produced IN738LC alloy shows solidification cracks all across the build.

Although tensile stresses are required for crack formation, in the current paper we focus exclusively on the other necessary condition, the liquid film, and in particular on the role of minor solute enrichment to grain boundaries. We use APT coupled with targeted, microstructurally site-specific sample preparation and transmission Kikuchi diffraction (TKD) to analyze the chemical composition profile of alloying elements across grain boundaries of SLM-produced IN738LC with unambiguously identified misorientation. The chemical composition profile at high angle and low angle grain boundaries, with solidification cracks and devoid of cracks, are quantified. Additionally, we compare the GB enrichment in the bottom layer and the topmost layer (i.e., material with and without the influence of remelting and reheating). The GB enrichment profile study on a modified IN738LC alloy with reduced content of Zr and Si (at least 60 wt. %) is also performed to understand the effect of these elements on crack suppression. These results are discussed in terms of the last stage of solidification and are further used to rationalize the contribution of microsegregation and solid-state segregation, especially of minor solute elements, to the GB enrichment profile. Finally, we critically evaluate the increase in the solidification interval (ΔT), due to interdendritic solute enrichment, on the solidification cracking mechanism.

II. EXPERIMENTAL METHODS

A. Additive manufacturing

The IN738LC samples used in this paper were produced from gas-atomized metal powder (Praxair Surface Technology GmbH, Germany). The particle size of the powder was in the range of 15–45 μm, a usual powder size for the SLM process [46]. Figure 1(a) shows a scanning electron microscopy (SEM) micrograph of the gas atomized IN738LC powder. The particles had spherical morphology. The micrograph of a polished cross section of a particle in Fig. 1(b) reveals a dendritic microstructure. The samples were manufactured on a modified TrumaForm LF250 (Trumpf, Germany). The SLM system is equipped with a multimode yttrium aluminum garnet laser source with a maximum output power of 470 W and a wavelength of 1070 nm. The laser spot size is approximately 94 μm. Cube-shaped samples of 1000 mm^3 dimension with wedges as support structures were built on a stainless-steel base plate at room temperature. The process chamber was maintained under inert gas atmosphere using argon, and the O_2 content was between 50 and 80 ppm. The samples were manufactured using a hatch spacing of 75 μm, a laser power of 135 W, a scan speed of 1000 mm/s, and a layer thickness of 20 μm. A stripe scan strategy as shown in Fig. 1(c) was employed. A scan rotation of 67° was performed between layers for homogenous energy input and to randomize crystallographic texture. Table II shows the chemical composition (at. %) of the powder and sample in the as-built condition which was analyzed by inductively coupled plasma and optical emission spectroscopy.

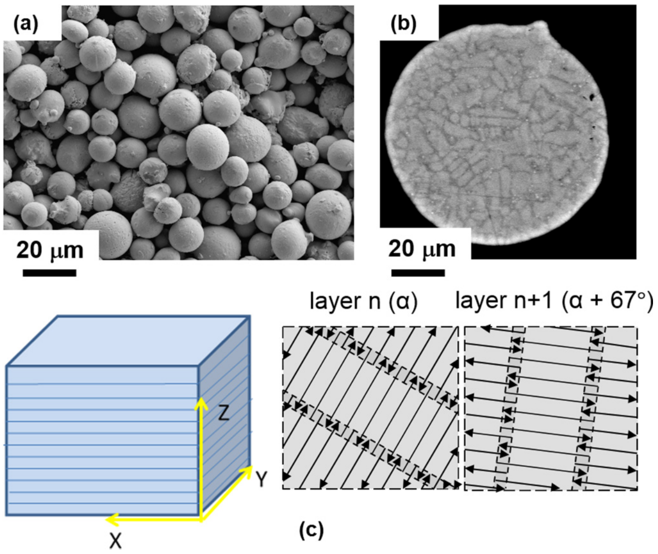

FIG. 1. SEM micrograph of (a) gas atomized IN738LC powders, showing a spherical morphology with a small number of satellites; (b) a polished and etched cross section, showing a dendritic morphology; and (c) the schematic of the “strip” scan strategy with a scan vector rotation of 67° between subsequent layers.

B. Analytical methods

The SLM-produced samples were mechanically polished using standard metallographic techniques. Electron backscattered diffraction (EBSD) analyses were performed in a Zeiss 1540XB cross beam FIB-SEM equipped with a Gemini field emission gun electron column, EDAX Hikari camera, and TSL-OIM Analysis EBSD data collection system. An acceleration voltage of 15 kV and a step size of 100 nm were used for the EBSD scans. The TSL-OIM analysis 7.2 software served for data postprocessing to identify the grain boundaries of interest, required for further atom probe measurements. Cleanup of the data was done using a grain confidence index (CI) standardization algorithm with a tolerance angle of 5°, a single iteration grain dilation algorithm, and a CI $>$ 0.1 [47]. SEM-energy dispersive x-ray spectroscopy (EDS) measurements were carried out in a Zeiss Merlin (Carl Zeiss SMT AG, Germany) to assess the elemental partitioning at the dendritic boundaries close to the crack. Site-specific specimen preparation for APT analysis of the grain boundary was performed using a standard lift-out procedure [48] in a FEI Helios Nanolab 600i FIB/SEM Dual Beam device, equipped with an OmniProbe micromanipulator. APT specimens were prepared using a silicon microtip coupon as support and sharpened using annular milling patterns at an acceleration voltage of 30 kV and focused ion beam (FIB) currents varying from 0.26 nA for the largest ring pattern to 46 pA for the smallest ring pattern. TKD measurement on the APT specimens was

TABLE II. The chemical composition (in at. %) of (a) IN738LC powders and (b) SLM-produced IN738LC standard samples.

Sample	Cr	Co	Al	Ti	W	Ta	Mo	Nb	C	Zr	Si	B	Ni
Powder	17.8	8.4	7.5	3.2	1.07	0.6	1.03	0.52	0.47	0.04	0.14	0.005	Bal.
As SLM produced	17.0	8.1	7.2	4.0	0.83	0.55	1.0	0.52	0.47	0.04	0.1	0.05	Bal.

done using an EDAX/TSL EBSD system in the FIB/SEM dual beam microscope, with a step size of 20 nm, to characterize the grain boundary misorientation. An explanation of this technique can be found in [49,50]. The same data analysis procedure, as stated above, was used. Post-TKD, the final tip sharpening was done at 5 kV and 23 pA to minimize Ga contamination at the surface.

The APT experiments were carried out in a local electrode atom probe (LEAP 3000X HR, CAMECA Instruments), which includes a reflectron for achieving high mass-to-charge resolution through flight path enhancement [51]. To prevent premature sample fracture, the APT tips containing grain boundaries were analyzed in pulsed-laser mode. The specimen temperature was maintained at ≈60 K with a target evaporation rate of 0.3%, laser pulse energy of 0.8 nJ, and laser pulse frequency of 250 kHz. The 3D reconstruction of the APT data was performed using CAMECA's IVAS software package (version 3.6.14). Cylinder dimensions for all the one-dimensional (1D) composition measurements were kept constant at 30-nm length and 10-nm diameter. The arrows inside the region of interest (ROI) cylinder represent the direction along which the 1D composition of the elements is calculated. All error bars represent a 2σ deviation. The dashed lines in all the graphs are the thicknesses of the isoconcentration surface (in at. % of either B or Zr) indicating the region of the grain boundary and its surrounding vicinity. Since local magnification effects and aberrations in ion trajectories can alter the local point densities in APT reconstructions, direct comparison of GB concentrations could be erroneous [52,53]. Hence, the Gibbsian interfacial excess value, Γ_x, of solute atoms (atom X per grain boundary area in square nanometers) has been calculated for all GB-APT measurements using the ladder diagram approach [54]. The Gibbsian interfacial excess of B, C, Zr, and Si in all the GBs is plotted as a histogram.

For TEM analysis, 3-mm-diameter cylindrical samples were cut by spark erosion, along the BD. Subsequently, 800-μm-thick disks were cut from the cylinder and mechanically thinned to less than 100 μm, followed by electropolishing until perforation. Electropolishing was carried out using a Tenupol 5 double jet at -30° and a voltage of 20 V, using an electrolyte of 70 vol % methanol, 20 vol % glycerin, and 10 vol % perchloric acid. Scanning transmission electron microscopy (STEM)-EDS analysis was carried out on a JEOL JEM-2200FS microscope operated at 200 kV.

III. RESULTS

A. Microstructure of as-SLM-produced samples

Figure 2(a) is an SLM sample in as-built condition. Figures 2(b) and 2(c) are optical micrographs of an SLM-produced sample showing cracks along the BD. This is a test sample that was produced at a laser power of 200 W, corresponding to an energy density (E_v) of 133 J/mm^3. All other process parameters were kept constant. This high-energy-density trial experiment with the SLM process was intentionally used to induce numerous cracks in the sample. Most cracks are parallel to the BD.

For the rest of the paper, the samples were produced with a laser power of 135 W and a laser scanning speed of 1000 mm/s (E_v of 96 J/mm^3). This is the optimized process parameter window, where defects such as cracks, lack of fusion, and balling were found to be at their minima. Figure 2(c) is a representative microstructure along the BD of one such

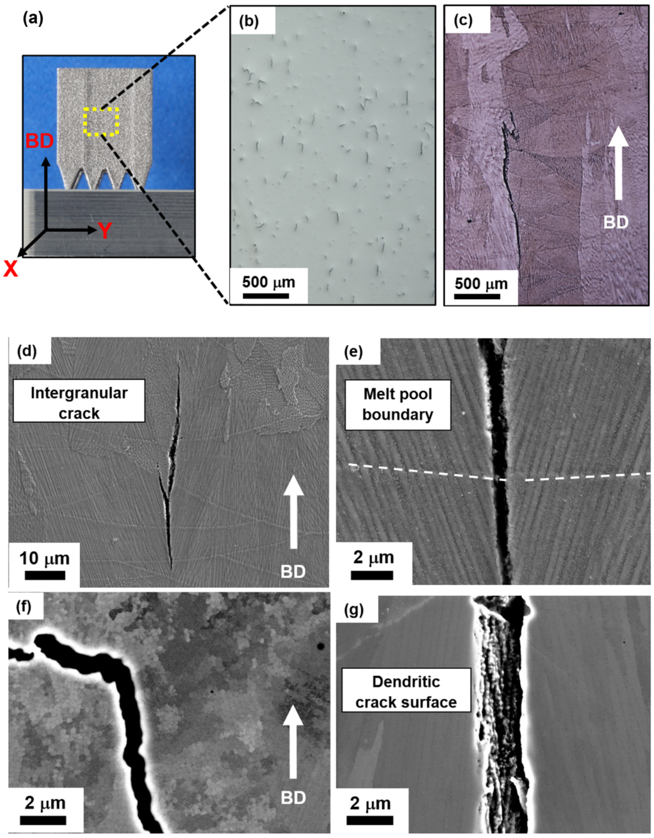

FIG. 2. (a) The as-built SLM sample. (b) Optical micrographs of an IN738LC SLM sample, produced with a higher laser power of 200 W, showing solidification cracks along the axis of the build direction (BD). (c) Representative microstructure along the BD of one such sample after etching in Adler's reagent. (d, e) SEM micrographs of intergranular cracks along the BD in samples produced with a laser power of 135 W. The sample is macroetched using Marble's reagent to reveal the solidification microstructure, showing large and elongated columnar grain morphology. (f, g) SEM micrographs showing solidification cracks in an unetched condition. The solidification cracks have a wavy structure with the crack surfaces complementary to each other, and the inner crack surface is dendritic in nature.

sample after etching in Adler's reagent. The cracks are intergranular in nature and extend over many melt pool borders, as seen in the etched microstructure. The crack density analyzed along the BD, defined as $\frac{\Sigma\text{ Length of a crack}}{\text{Area of analysis}}$, is 3.4 mm^{-1}. Figures 2(d) and 2(e) show the SEM micrographs of intergranular cracks. A characteristic epitaxial type of dendritic growth along the BD is observed, similar to previous observations in as-SLM-produced microstructures of IN738LC [21,22,55,56].

Figures 2(f) and 2(g) are SEM micrographs of a microcrack in an unetched condition. Figure 2(e) shows that these microcracks have a wavy structure with the crack surfaces complementary to each other. On the crack surface (extending into the specimen), dendritic structures are clearly visible [Fig. 2(g)].

Although the formation of γ' precipitates is expected both from common knowledge of as-cast microstructures and from thermodynamic calculations [57] (using Thermo-Calc and TTNI8 database), we do not detect any in the current microstructure by SEM probing. The fine primary dendritic arm spacing indicates a high cooling rate (10^4–10^6 K/s) during the SLM process [56–59], a value so high that it might be responsible for suppressing γ' precipitation. The only precipitates in the microstructure are carbides. They are found predominantly in the interdendritic regions. These carbides are Ti-rich MC-type carbides (see Sec. III B 3) and form from the last remaining interdendritic liquid. The absence of low-melting phases, as well as the crack surface morphology, strongly suggest that the observed cracks are formed as solidification cracks along grain boundaries [12,13].

We measured the misorientation across 126 cracks chosen randomly along the BD by individual EBSD scans together with the corresponding crack length.

Figure 3 shows a scatter plot of the misorientation versus the crack length. It reveals that cracks are exclusively formed on high angle grain boundaries (15°–60°) and not on low angle grain boundaries (5°–15°). The Brandon criterion [60] analysis shows that none of the grain boundaries exhibited any low-index coincidence or near-coincidence site lattice (CSL) relationship. Brandon's criterion states that interfaces with sufficiently small deviations from exact CSL angles can still be considered as CSL boundaries as the misfit is in such cases assumed to be accommodated by a secondary grain boundary dislocation array. The current observation that the as-built microstructures are devoid of CSL interfaces agrees well with corresponding findings for the grain boundary character of solidification cracks during welding and casting in superalloys [14,30,34]. The crack length varies between 25 and 275 μm, and the average crack length is 68 μm.

B. Chemical composition of grain boundaries and carbides

Figure 4(a) is an SEM micrograph of a randomly selected crack, overlaid with the grain boundary misorientation map obtained by EBSD. This particular crack is along a HAGB with a misorientation of 48° around the [14 13 9] rotation axis. Figures 4(b)–4(e) show EDS maps of the region of interest close to the crack. The elemental distribution maps of Ni, Cr, Co, and Al do not exhibit any enrichment at the interdendritic boundaries and hence are not shown. In contrast, Ti, along with Nb and Mo, shows strong enrichment in the interdendritic regions. The feature strongly enriched in Ti but not Nb or Mo is a pore, possibly covered by titanium oxide. The EDS maps also confirm the absence of any second phases at this magnification.

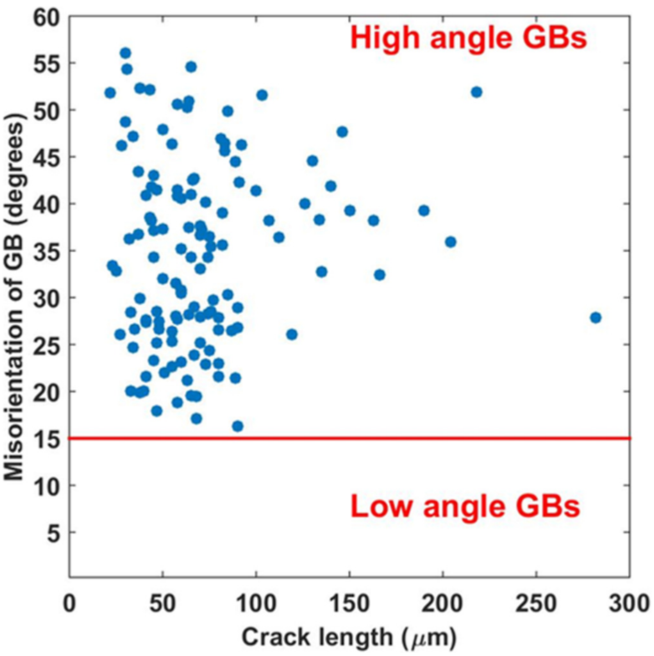

FIG. 3. Plot of the grain boundary misorientation vs crack length, from the EBSD misorientation analysis of 126 cracks chosen randomly along the build axis, BD. All solidification cracks are formed on the high angle grain boundaries (15° – 60°) only. The crack length varies between 25 and 275 μm, and the average length of the cracks is 68 μm.

To study the elemental distribution at the interdendritic regions in more detail, STEM-EDS mapping was performed. The STEM micrograph, together with EDS elemental maps in Fig. 5, shows carbides in the interdendritic regions. They have an ellipsoidal shape with a length of up to 20 nm. STEM-EDS maps reveal that the carbides are depleted in Ni, Al, Co, and Cr and enriched in Ti, Ta, W, Mo, Nb, Si, and Zr (see white arrows). Importantly, the enrichment of Ti at the solidification cell boundaries (typically subgrain boundaries) is much broader than that of the other elements, with a width of around 100 nm. The enrichment of W, Ta, Mo, Nb, Zr, and Si is restricted only to the carbides at this magnification.

In the TEM investigation, we could neither unambiguously determine differences in elemental enrichment along the LAGB and HAGB nor ascertain the enrichment of the minor alloying elements such as Si and Zr that play a crucial role in solidification cracking. Element distribution maps of Ta and W are affected by the strong overlap of their characteristic x-ray energies. Hence, systematic APT investigations of grain boundaries of different types were performed. Out of the total number of ten analyzed GBs, we present three different measurements in detail: (a) a HAGB that is devoid of any cracks (but adjacent to a crack), (b) a HAGB in front of a solidification crack, and (c) a LAGB (uncracked). Specimens for these APT measurements were extracted from regions close to the crack, as shown in Fig. 4(a). Additionally, we

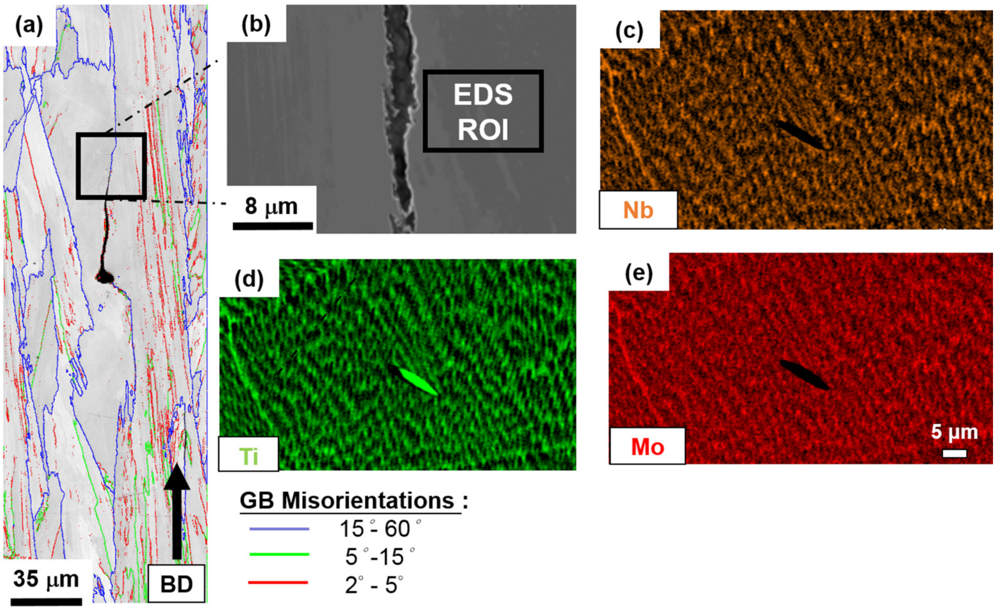

FIG. 4. (a) EBSD grain boundary map obtained along the build direction (BD) showing the various high angle grain boundaries (in blue, misorientation criteria > 15°) and low angle grain boundaries (in green, misorientation criteria 5° − 15°). The solidification crack is on the high angle grain boundary with a misorientation of 48° [14 13 9]. (b–e) EDS maps of the interdendritic enrichment of Nb, Ti, and Mo at the region of interest (ROI) close to the crack.

analyzed APT datasets from two more HAGBs in front of cracks at other locations, from a second LAGB and from three HAGBs (without cracks) located in the very last deposited layer. These latter experiments are discussed in terms of the Gibbsian interfacial excess of alloying elements only.

1. APT measurements on a HAGB without a crack

Site-specific lift-out to prepare APT specimens was made from a grain boundary the misorientation of which is 30° around [1 1 19] without a solidification crack. Figure 6(a) is an SEM image of the APT specimen before final tip sharpening.

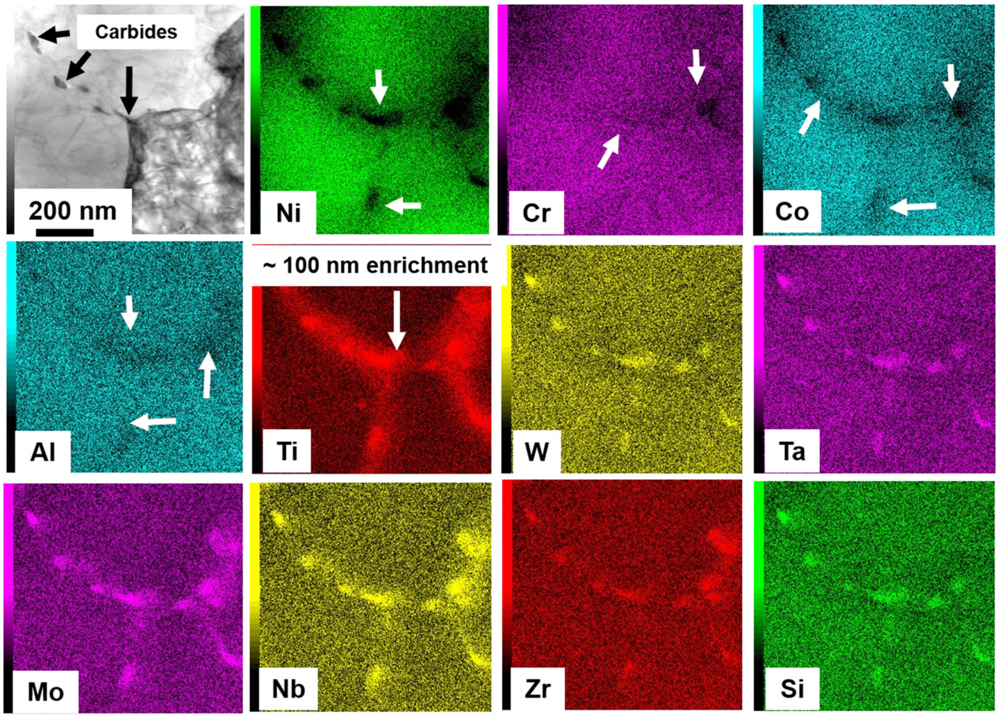

FIG. 5. STEM-EDX maps revealing the enrichment of Ti, Ta, W, Mo, Nb, Si, and Zr in the carbides and depletion of Ni, Cr, Co, and Al (white arrows). The enrichment of Ti at the cell boundaries is with a width of around 100 nm, while the distribution of W, Ta, Mo, Nb, Zr, and Si is restricted only to the carbide precipitates.

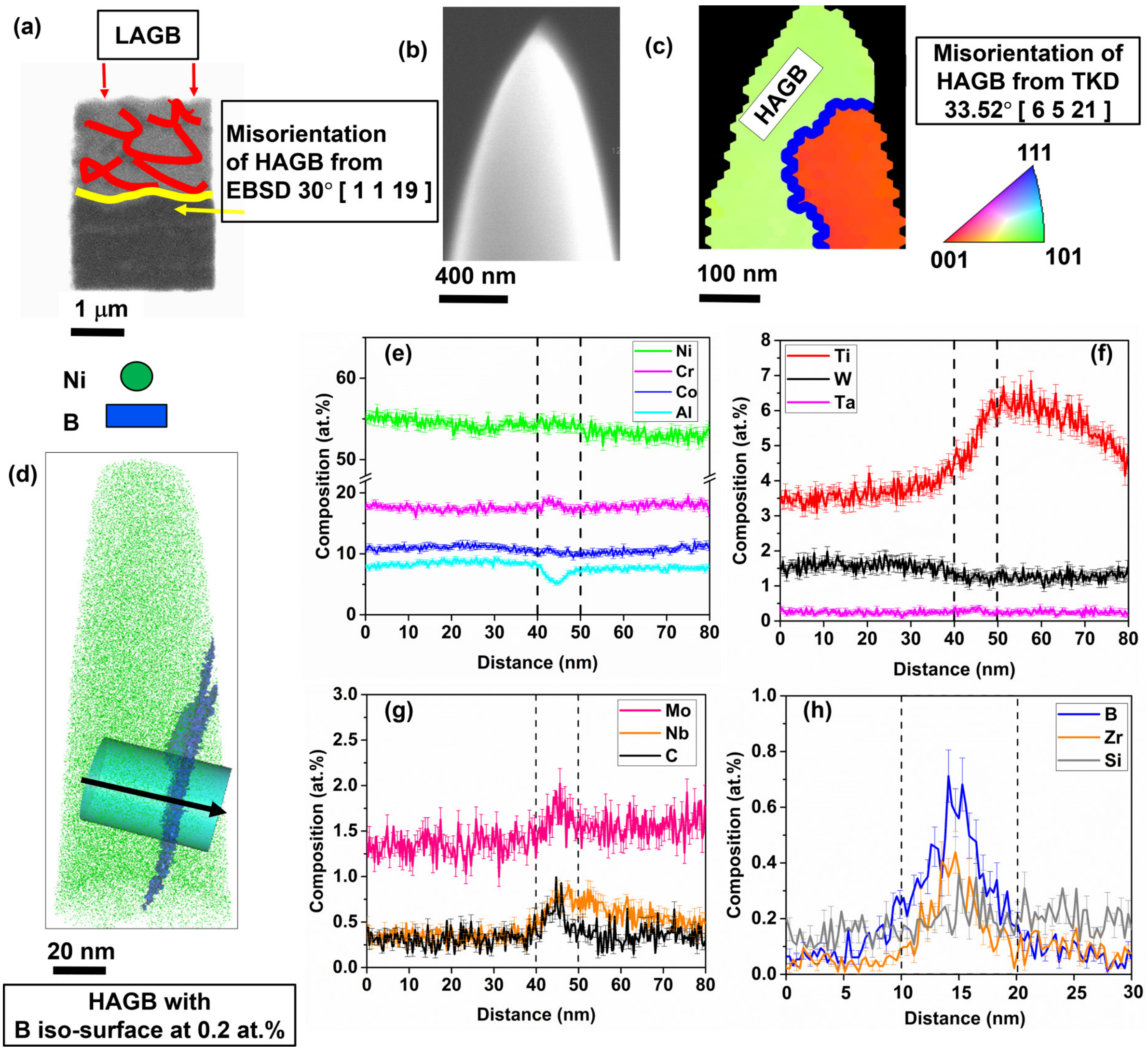

FIG. 6. (a–c) APT lift-out sequence for a high angle grain boundary (HAGB) next to a solidification crack the misorientation of which is 30° [1 1 19]. (a) SEM image of the lamella on the Si microtip. A network of subgrain boundaries, which are typically low angle grain boundaries (in red), is seen close to the HAGB of interest (in yellow). (b) APT specimen. (c) TKD map of the atom probe specimen showing the grain boundary in blue. The misorientation of this boundary from the TKD map is 33° [6 5 21]. (d) Reconstructed atom maps of the HAGB. (e–h) 1D composition profile of all the elements across the HAGB quantified using the ROI cylinder. The vertical dashed lines indicate the region of the GB and the surrounding vicinity.

A network of LAGBs (i.e., dendrite boundaries, highlighted in red) is seen close to the HAGB of interest (in yellow). To draw reliable conclusions, the presence of the GB of interest was confirmed by performing an additional TKD measurement on the final APT specimen. The TKD map in Fig. 6(c) shows that the misorientation of the HAGB (blue) in the APT specimen (33° [6 5 21]) is consistent with the EBSD measurement before APT specimen extraction. Figure 6(d) is a reconstructed APT data set with only Ni atoms (shown in green). The HAGB is highlighted by a 0.2-at.-% B isoconcentration surface (in blue). The 1D composition profiles along the axis of the cylinder shown across the GB are calculated and shown in Figs. 6(e)–6(h). Ni, Cr, Co, and W are homogeneously distributed across the HAGB. There is a depletion of Al at the HAGB down to 5 at. %. Ti, Ta, Mo, Nb, C, B, Zr, and Si are enriched at the HAGB. Interestingly, the Ti and the Nb enrichments across the HAGB are much broader, resembling an "S-shaped" profile and with an asymmetric distribution. The width of Ti and Nb enrichment profiles is ≈80 nm, much broader than the profiles of the other elements. This broad Ti enrichment agrees with the STEM-EDS measurements at the cell boundaries (Fig. 5).

2. APT measurements on a HAGB in front of a solidification crack

Figures 7(a) and 7(b) show a similar APT lift-out and TKD measurement from the HAGB in front of a solidification crack. The misorientation of the HAGB from the TKD measurement is 53° [16 4 23]. Figure 7(a) shows the location of the APT specimen lift-out in front of the crack tip. The 1D composition profiles of selected elements across the HAGB are shown in Figs. 7(d)–7(f). Unlike the previous measurement, Al does not show a depletion, and W shows some enrichment at the GB. Ta is homogenous across the GB. Ti exhibits a similar S-shaped enrichment profile across the

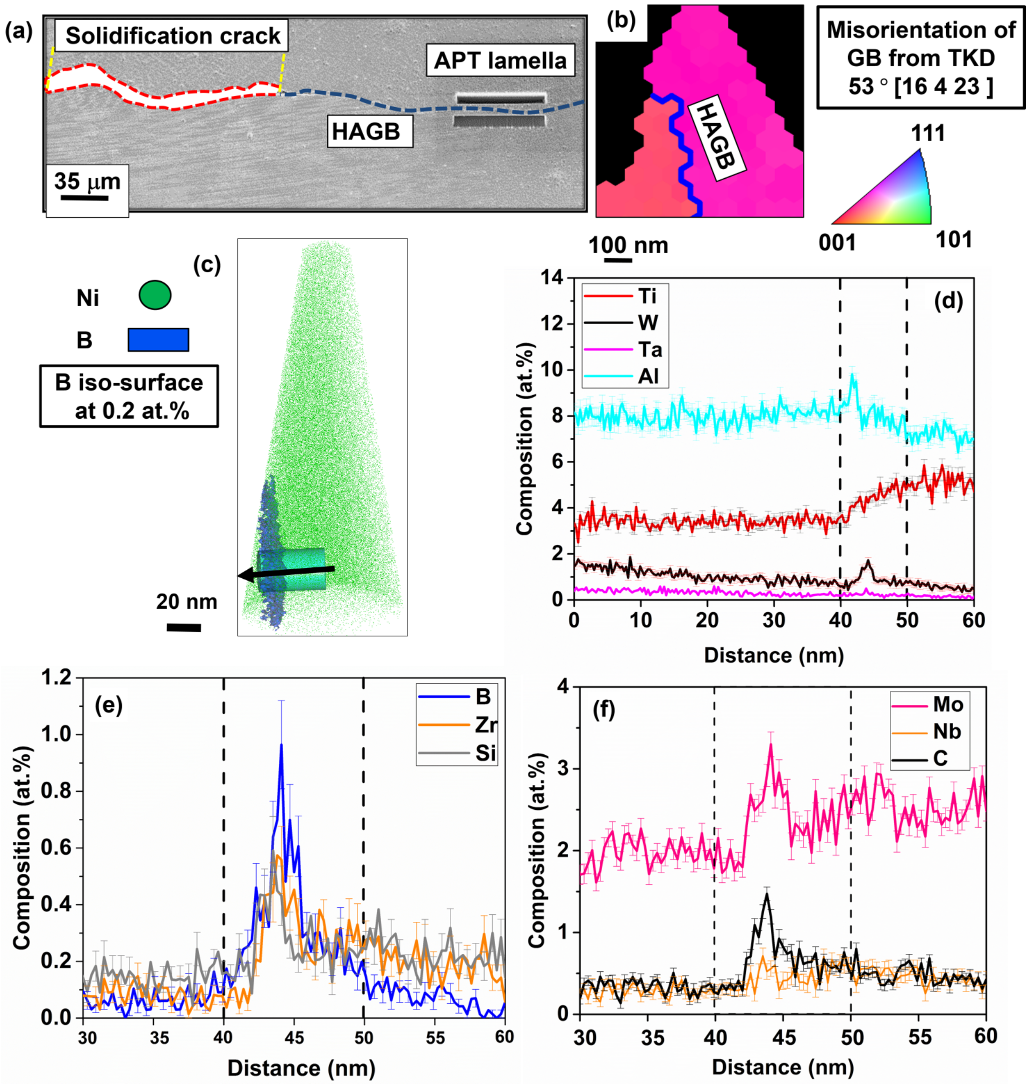

FIG. 7. (a) APT lift-out sequence for a high angle grain boundary (HAGB) in front of a solidification crack, the misorientation of which is 48° [14 3 19]. (b) TKD map of the atom probe specimen showing the grain boundary in blue. The misorientation of this boundary from the TKD map is 53° [16 4 23]. (c) APT reconstruction of Ni atoms with a 0.2-at.-% B isoconcentration surface at the HAGB. (d–f) 1D composition profile of selected elements across the HAGB quantified using the ROI cylinder. The vertical dashed lines indicate the region of the GB and the surrounding vicinity.

HAGB [Fig. 7(d)]. Since in this dataset the grain boundary is very close to the edge of the specimen we do not see the complete S-shaped profile. Otherwise, and somewhat surprisingly, the enrichment of the minor alloying elements, such as B, C, Zr, and Si, across this HAGB, is almost identical to the HAGB without a crack.

3. *Atom probe measurements on a low angle grain boundary*

Figure 8(a) is the TKD map of a LAGB having a misorientation of 6° [19 6 20]. The atom maps of C and Ti are also shown. A Ti-rich carbide is present at the interface of the LAGB. Figure 8(b) also shows the LAGB as an isosurface of 0.2-at.-% B. A closer analysis of the carbide precipitation behavior will be further investigated in a separate study. The 1D composition profile analysis is done only along the LAGB, 20 nm away from the carbide and therefore not influenced by it. As in the HAGB cases, there is no enrichment or depletion of Ni, Co, Cr, and Al across the boundary. Figures 8(c) and 8(e) are 1D composition profiles of the minor elements across the LAGB. B and C are in excess at the LAGB, similar to the HAGB case. Interestingly, the compositions of W [Fig. 8(d)], and in particular Zr and Si, are constant across the LAGB, unlike in the HAGB case.

C. Modified alloy IN738LC: Reduced zirconium and silicon content

Previous APT results demonstrate the difference in enrichment, particularly for minor alloying elements, between LAGB and HAGB. A set of SLM experiments with identical process parameters was performed using a modified IN738LC powder with reduced Zr and Si content. The Zr content was reduced from 0.06 to 0.02 wt. % and the Si content was reduced from 0.07 to 0.01 wt. %.

The SEM micrograph [Fig. 9(a)] of the as-SLM-produced modified alloy, with reduced Zr-Si content, clearly shows

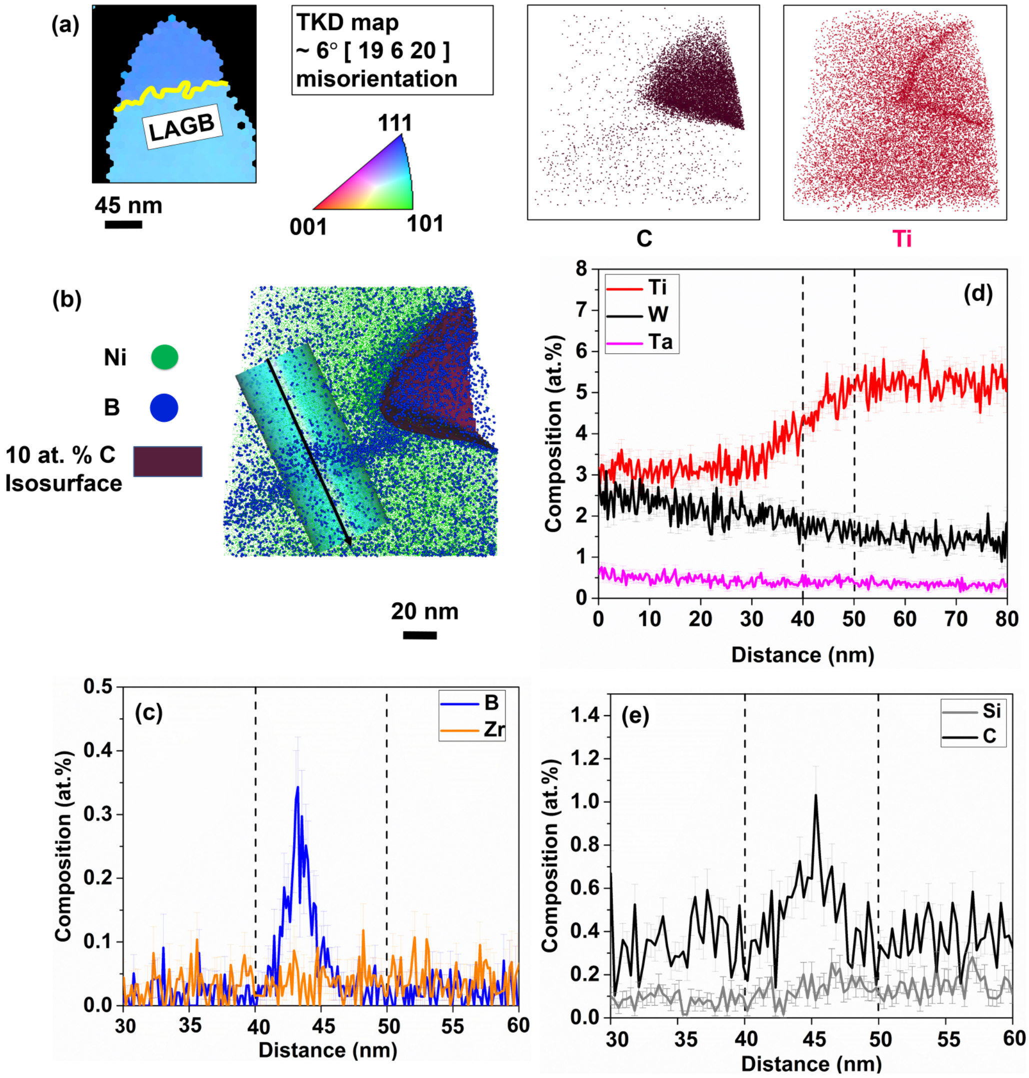

FIG. 8. (a) TKD map of the atom probe specimen showing the low angle grain boundary (LAGB) in yellow, with a 6° [19 6 20] misorientation and the corresponding APT reconstruction of a Ti-rich carbide at the LAGB (Ti and C atom maps). (b) APT reconstruction of Ni atoms with the LAGB highlighted as B atoms (in blue) and carbide precipitate shown as a 10-at.-% C isoconcentration surface. (c–e) 1D composition profile of selected solute species across the LAGB quantified using the ROI cylinder. The vertical dashed lines indicate the region of the GB and the surrounding vicinity.

complete disappearance of the solidification cracks. We analyzed a HAGB (30.3° [2 2 21] misorientation) by APT and TKD. Figures 9(d) and 9(e) show the 1D composition profile comparisons between the HAGBs of the standard alloy (replotting the data presented in Figs. 6 and 7) and the low Zr–low Si alloy. The reduction in the bulk Zr and Si content (by 66 and 85 wt. %, respectively) in the SLM-produced alloy apparently did not suppress their respective enrichment at the HAGB. All the APT results are summarized as bar charts of the Gibbsian excess of selected elements (B, C, Zr, and Si) in Fig. 10.

IV. DISCUSSION

A. Microsegregation versus solid-state segregation

The enrichment of minor alloying elements to defects such as grain boundaries in superalloys influences the material's macroscopic properties [61,62]. Solute enrichment at interfaces is either due to solid-state diffusion and equilibrium segregation (postsolidification) or due to solute partitioning during solidification, termed microsegregation. In the latter case, solute enrichment occurs by partitioning to the liquid phase, in the interdendritic regions, before grain boundaries form upon final solidification.

Microsegregation can be of equilibrium or nonequilibrium type, depending on the solidification conditions. Under relatively slow solidification conditions, an equilibrium partitioning of solute between solid and liquid phases occurs. In contrast, in nonequilibrium solidification, solute partitioning is a function of the solid-liquid interface velocity [36]. In the extreme case of rapid solidification, solute trapping leads to microsegregation-free solidification. At intermediate solidification rates, the solute composition profile, resulting from microsegregation, is influenced by solute diffusion rates in the liquid and solid phases. The composition gradients are highest where the last remaining liquid solidifies, i.e., at the

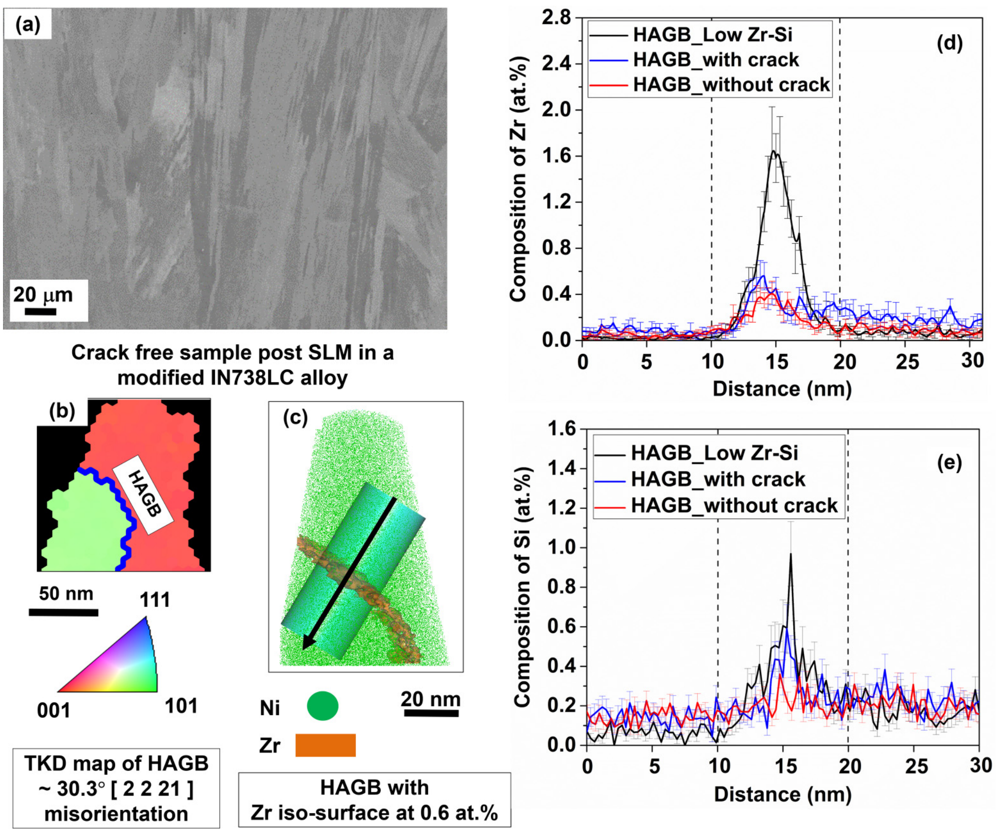

FIG. 9. (a) SEM image of the microstructure along the build direction of a modified IN738LC alloy. (b) TKD map of the atom probe specimen showing the HAGB in blue, with a 30.3° [2 2 21] misorientation. (c) APT reconstruction of Ni atoms with a Zr isoconcentration surface of 0.6 at. % at HAGB. (d, e) 1D composition profile comparisons between the HAGBs of the standard alloy and the low Zr–low Si alloy. The enrichment of Zr and Si at the HAGB of the modified alloy is higher than their respective enrichments in the standard IN738LC alloy composition.

site of emerging GBs [35]. Microsegregation of solute to interdendritic regions contributes to the solidification cracking susceptibility [63].

The microsegregation models initially proposed by Scheil and Gulliver assume equilibrium solute partitioning into the liquid, no diffusion in the solid state, and complete mixing in the liquid. However, during solidification there is a redistribution of solute from the liquid to the solid phase, referred to as back-diffusion [36,64]. The concept of back-diffusion has been numerically incorporated in microsegregation theories in different ways [65–68].

Models developed later [69–72] also take into consideration the limited diffusion rate in the liquid, giving rise to solute composition gradients, important during rapid solidification [73]. The simplest analysis of microsegregation is based on the partition coefficient, k, and the solid-state diffusivity, D_s [8]. A value of $k < 1$ implies a tendency of the solute to partition to the liquid during solidification. A high value of D_s of a certain species leads to a greater degree of back-diffusion of the particular solute from the liquid into the solid during solidification and therefore leads to a wider, less pronounced segregation profile across the GB [14].

Contrary to microsegregation during solidification, equilibrium segregation of solute atoms to GBs occurs in the solid state, typically during heat treatment at temperatures where substantial solid-state diffusion can occur. This segregation reduces the overall GB energy [61]. Theoretical formulations of the diffusion-mediated chemical segregation from the surrounding solid into the GBs have been given in [61,74,75]. The extent to which thermodynamically favorable segregation can occur is determined by the diffusivity of species in solid, D_s, together with the local time-temperature profile experienced by the material.

Solidification cracking in the current paper occurs while there is still remaining liquid in the interdendritic regions present, i.e., where two dendrites are going to merge and form a GB. However, the observed composition profiles at GBs occur after complete solidification and cooling down. Hence, it can have been created by both microsegregation and solid-state segregation.

Scheil-Gulliver thermodynamic calculations using Thermo-Calc with the TTNI8 database for Ni-base superalloys, including liquid, γ, and carbide phases, were performed to evaluate the liquid composition as a function of temperature. The composition plots for all the solute elements can be found in Figs. 11(a)–11(c). Importantly, the calculations predict a strong partitioning of minor solutes, B, Zr, and Si, into the liquid at the last stage of solidification, equivalent to ≈3.6, 3.2, and 0.5 at. %, respectively. This is in general agreement with our measured APT compositional profiles across HAGBs and LAGBs. However, the APT results reveal that the B enrichment is

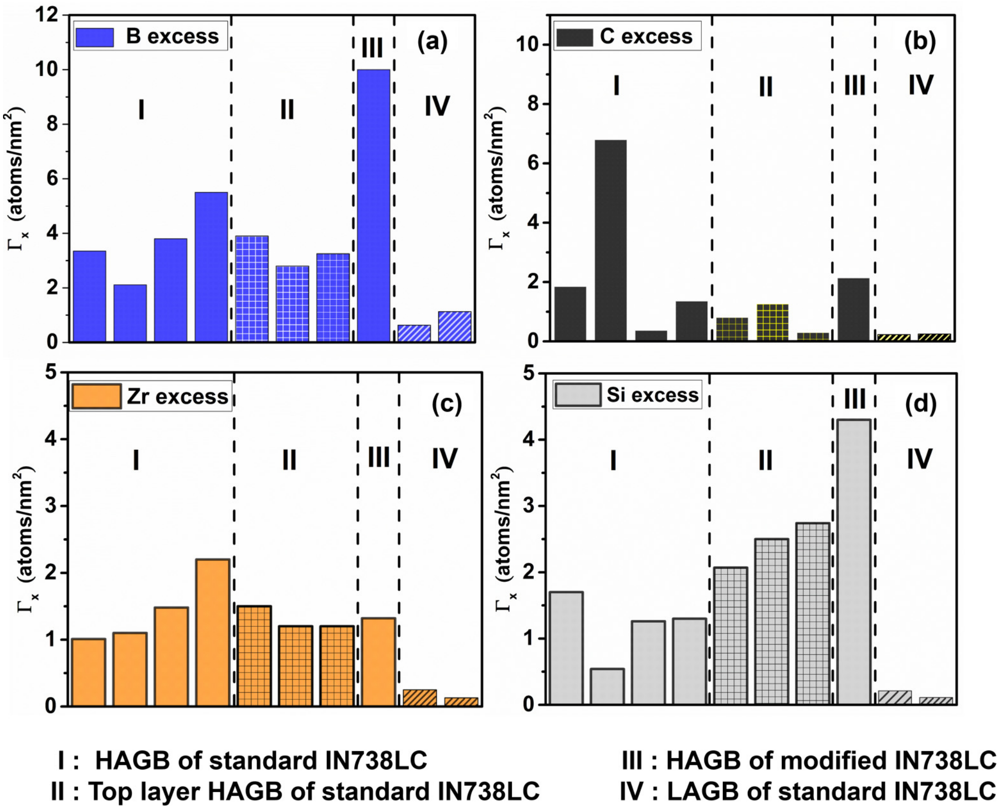

FIG. 10. Plots showing the variation in calculated Gibbsian interfacial excess from APT in different HAGBs and LAGBs for (a) B, (b) C, (c) Zr, and (d) Si. The plots show a consistently higher excess of Zr and Si in the HAGBs as compared to LAGBs. The modified IN738LC alloy has a higher excess of Zr and Si as compared to the standard alloys. Also, the GB excess of Zr and Si at the HAGBs, in the top layer (see Supplemental Material [80]), is similar to the HAGBs in the bottom layers.

approximately three times lower and C is ten times higher than the compositions predicted by the calculation. In contrast, at HAGBs, the Zr content is approximately three times above the predicted compositions, whereas the Si content (0.5 at. %) is nearly consistent between experiment and simulation. As discussed earlier, LAGBs are not enriched in either Zr or Si. These discrepancies demonstrate that the difference in the enrichment of minor solutes to HAGBs and LAGBs must be taken into account during the prediction of solute enrichment. This distinction cannot be made by simple Scheil-Gulliver calculations.

For the solute species of IN738LC, the solid-state diffusion coefficients (D_s) at various temperatures were calculated using the Arrhenius equation. The preexponential factors (D_0) and the activation energy (Q) for diffusion were taken from the literature [76–78] (see Supplemental Material [79]). To approximate the diffusion distance (x) of various atomic species during cooling down until complete solidification, we numerically integrate the equation, $\sqrt{\langle x^2 \rangle} = \sqrt{\langle 6D_s t \rangle}$. We assume a cooling rate of 10^6 K/s (a high assumption) and a solidus temperature of 1300 K (a low assumption). This choice of values leads to a calculated diffusion distance that is at the lower end of the range of values to be expected (see Supplemental Material [79]). The numerical values on the top of each bar graph are the absolute values of the predicted distances in nanometers.

Figure 12 shows the diffusion distances of the solute species C, B, Zr, Si, Ti, and Nb. The calculations predict that B, C, and Zr, being fast diffusers in Ni, can redistribute in a wide region adjacent to the grain boundary during cooling, despite the very high cooling rates of SLM. The minimum calculated diffusion distance in this group of elements is 170 nm. Slow-diffusing elements such as Si, Ti, and Nb have a solid-state redistribution range of only around 1 nm after 10^6 s at 330 K. These calculations suggest that the final GB chemistry, after full solidification, measured by APT [cf. Figs. 13(a)–13(f)] is influenced by both microsegregation and solid-state segregation.

This behavior is clearly species dependent: B, C, and Zr profiles [Figs. 13(a)–13(c)] are expected to be heavily influenced by solid-state diffusion to or from the GB. However, the composition profiles across the GB of Si, Ti, and Nb should be practically completely due to microsegregation [Figs. 13(d)–13(f)]. This solute-specific behavior may explain the different shape of the composition profiles of some of the elements. Due to its origin from microsegregation, the Ti and Nb profiles are much broader than, e.g., the Zr profile, which results from solid-state GB segregation. Note that also microsegregation can lead to very sharp composition profiles if the solute is concentrated very strongly in the last remaining liquid, as is the case for Si [Fig. 13(d)]. The asymmetric composition profiles of Ti and Nb [Figs. 13(e) and 13(f)], however, cannot be explained by conventional microsegregation models with isotropic solid-liquid interface energies.

Harrison *et al.* [9] attribute the inhibition of intergranular segregation of Si to rapid solidification conditions and solute

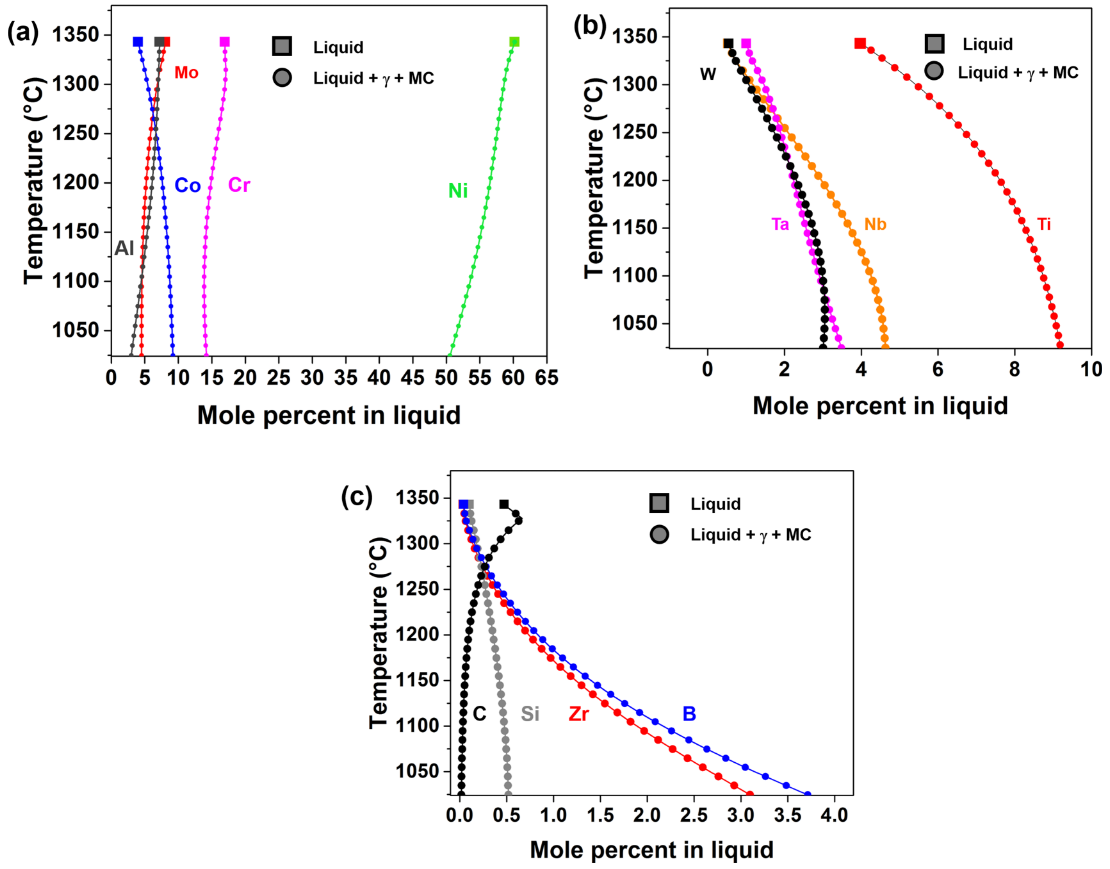

FIG. 11. (a–c) Plots showing the calculated evolution of solute enrichment in the liquid phase as a function of temperature using Scheil-Gulliver assumptions. The calculations were performed using the Thermo-Calc with the TTNI8 database.

trapping during SLM of Hastelloy X. The authors perform SEM-EDS line scans to show the lack of segregation of Si at the intergranular crack surface. However, the GB excess plots in Fig. 10(d), obtained from the APT analysis, confirm that Si enrichment occurs at the HAGBs in IN738LC. We suspect that the characterization method employed by Harrison *et al.* precluded them from measuring a Si enrichment at GBs. For the current alloy system and process parameters, we cannot confirm the interpretation suggested in [9] that the SLM process is within the (complete) solute-trapping regime.

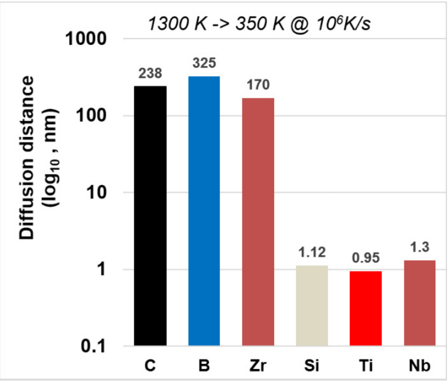

FIG. 12. Bar graph showing the predicted diffusion distances of solute elements such as C, B, Zr, Si, Ti, and Nb at 350 K. Details of the diffusion calculations are elucidated in nanometers.

B. Misorientation dependence of cracking

According to the experimental and theoretical evidence [34,35], the HAGBs (repulsive interfaces) have larger hot cracking susceptibility compared to LAGBs (attractive interfaces). Our experimental evidence of solidification cracks, only occurring on the HAGB of SLM-produced IN738LC, agrees with this description.

The theoretical model of Rappaz *et al.* [35] elucidates the effect of back-diffusion of solute from the remaining thin layer of interdendritic liquid, during the last stage of solidification, influencing its final coalescence behavior. The model predicts that for a remaining liquid at a repulsive interface an additional undercooling, ΔT_b, [as described in Eq. (1)] is required for final coalescence. Conversely, for an attractive interface, full solidification occurs at a higher temperature than predicted by the liquidus line.

The resulting undercooling required for a repulsive interface causes more back-diffusion of solute from the remaining liquid at the intergranular region. This back-diffusion of solute tends to lower the solute composition in the remaining liquid. The coupled effect of temperature reduction due to heat extraction and the reduction of the liquid composition due to back-diffusion drives the liquid to reach the coalescence temperature, hence completing the solidification process [33].

Figures 14(a) and 14(b) are the plots of the sharp-interface model predictions of the last stage of solidification in a model binary alloy adapted from [35]. The coalescence temperature is given by the dashed black line in Fig. 14(a), which is

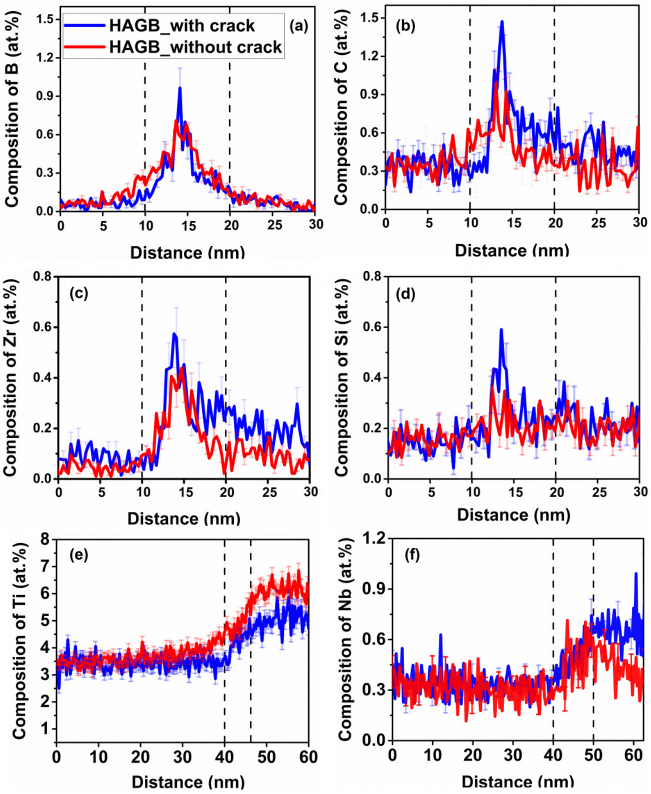

FIG. 13. (a–f) 1D composition plots comparing the enrichment profile of B, C, Zr, Si, Ti, and Nb across the two HAGBs. The grain boundary enrichments of the minor alloying elements (B, C, Zr, and Si) are similar in the HAGB with a solidification crack and the HAGB without a solidification crack.

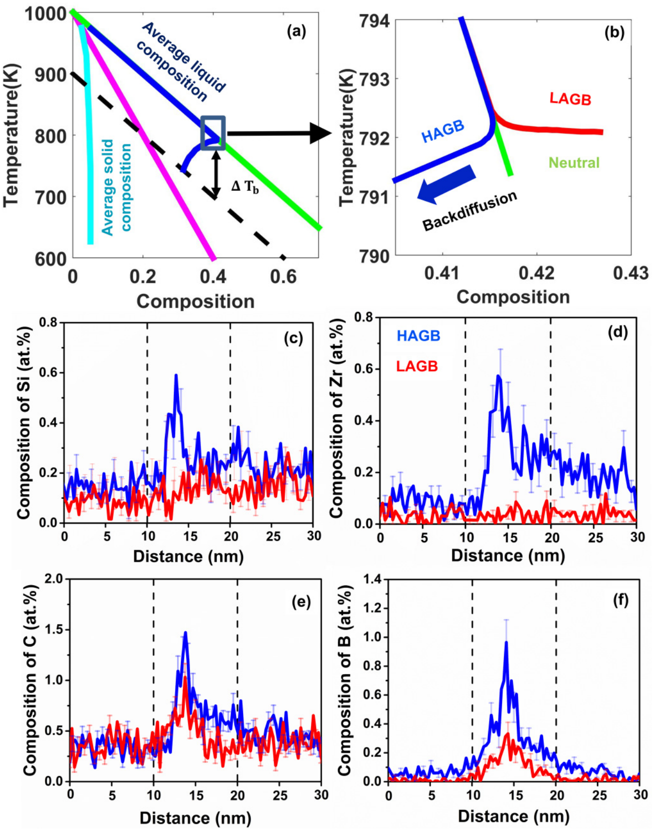

FIG. 14. Plots in (a) and (b), adapted from [29], are the sharp-interface model predictions of the last-stage solidification theory in a model binary alloy. The black dashed line in (a) is the coalescence line. (b) The influence of grain boundary energy on the nature of coalescence of the last liquid in an attractive (LAGB), neutral, and repulsive (HAGB) interface. (c–f) Experimentally obtained 1D composition profile comparing the enrichment of Si, Zr, C, and B in the HAGB and LAGB in SLM-produced IN738LC.

parallel to the liquidus line of the phase diagram, with a shift of ΔT_b (θ), governed by Eq. (1). The sharp-interface calculations predict that the composition of the remaining liquid for a HAGB [blue line, Fig. 14(b)] deviates from the liquidus to lower solute composition due to the back-diffusion of solute. At this temperature and reduced solute composition, the remaining liquid between the dendrites solidifies, marking the completion of solidification. For a neutral interface ($\gamma_{\text{GB}} = 2\gamma_{\text{sl}}$), the coalescence occurs on the liquidus line (in green). For an attractive interface, as the thickness of the liquid film decreases, theory predicts that the liquid composition terminates above the liquidus, at a higher composition (in red).

Figures 14(c)–14(f) summarize the 1D composition profiles of B, C, Zr, and Si at the HAGB and LAGB, respectively. The current APT and TKD study shows greater enrichment of Si and Zr at the HAGB as compared to the LAGB [Figs. 14(c) and 14(d)]. This is opposite to the prediction made by the above theory. It can be clearly seen that Zr and Si are enriched only at the HAGB and not in the LAGB. From the GB excess plots of Zr and Si [Figs. 10(c) and 10(d)], we consistently see higher excess of Zr and Si in HAGBs as compared to LAGBs. While our analysis of solid-state diffusion suggests that the measured composition profile of Zr is probably not the one existing right after solidification, the Si composition profile should be mostly unaffected by solid-state diffusion. Additionally, the GB excess of Zr and Si at the HAGB in the top layer (see Supplemental Material [80]) is similar to that at the HAGB in the bottom layers. Hence, the GB chemistry is not influenced by the multiple reheating cycles arising from the deposition of subsequent layers during the SLM process (“intrinsic heat treatment”).

The extent of back-diffusion of solute from the remaining liquid into the solid is sensitive to the local cooling rate, the length scale of the dendrites, and the solid diffusion coefficient (D_s). The degree of back-diffusion of an alloying element in Ni depends on its type of site occupancy, i.e., whether it is substitutional or interstitial [14]. Interstitial elements such as C and B have diffusion rates orders of magnitude higher than substitutional elements like Cr and Co in Ni [15,81] (see Supplemental Material [79]). In the current paper, we do not see such a direct correlation between the extent of back-diffusion and the GB enrichment profile. Though C and B have high mobility for back-diffusion, we see enrichment at both the HAGB and LAGB [Figs. 14(e) and 14(f)]. Si is a substitutional element [82], and Zr has a high diffusion coefficient of $\approx 10^{-11}$ m^2 s^{-1} in Ni, but they show different profiles in the HAGB and LAGB.

C. Effect of second phases

The formation of low-melting phases and liquation (remelting) of secondary precipitates at the GB is a plausible mechanism for initiating microcracks in laser-welded IN738LC samples [17,19]. Recent APT studies by Chauvet *et al.* [83] have reported traces of intergranular residual liquid enriched in B, close to the crack surface. However, in their selective electron-beam melting process, the final superalloy microstructure contained a significant fraction of γ' precipitates and borides, indicative of a much slower cooling rate than in our experiments. In the SLM-produced IN738LC investigated here, the SEM micrographs and subsequent APT analysis do not reveal any γ' or γ/γ' eutectics at grain boundaries. Therefore, the role of γ/γ' eutectics or residual liquid from borides and carbides, that are further stabilized by the minor solute elements, does not contribute to the solidification cracking.

Pertaining to the effect of Si enrichment at the GB in SLM-produced superalloys, Engeli *et al.* [37] and Tomus *et al.* [10] hypothesize that Si segregation could promote the formation of detrimental phases at GBs. Although the current APT-GB analysis reveals Si enrichment, there is no evidence of any detrimental Si-rich phases at any of the GBs. Only Ti-rich carbides are observed [Fig. 8(a)]. The carbides, however, are present at the dendritic and interdendritic regions and also on noncracked GB. Hence, they are not a plausible source of crack initiation.

D. Role of the solidification interval during the cracking process

A comparison of the Zr enrichment between the different GBs, both in standard and modified alloys, is plotted in Figs. 9(d) and 9(e). A similar Zr enrichment profile can be seen at all three types of GBs. In their interpretation of solidification cracking of SLM-produced IN738LC, Cloots *et al.* [8] follow the often-used assumption that there exists a critical temperature range (ΔT_{CTR}) for cracking, defined as $\Delta T_{\mathrm{CTR}} = T_{\mathrm{liquidus}} - T_{\mathrm{solidus}}$. This temperature range is suggested to mark the vulnerable regime for the initiation of cracks during alloy solidification. They quantify the enrichment of Zr at an unspecified GB (probably a HAGB) by one APT measurement and hypothesize that this could lead to a reduced solidus temperature of the last remaining liquid, prior to the formation of the GB. Consequently, the ΔT_{CTR} range increases by the same amount and this interdendritic liquid film, enriched with Zr, remains stable to low temperatures, leading to solidification cracks.

In the current paper, APT results show a Zr Gibbsian interfacial excess of 1.5 atoms/nm^2 at all the HAGBs [see Fig. 10(c)]. Crucially, in the modified low Zr-Si alloy, we find an interfacial excess of 1.2 atoms/nm^2 of Zr, at the HAGB, similar to its value at the HAGBs in the standard alloy. If the increase in the local GB solidification interval due to Zr enrichment (as postulated by Cloots *et al.* [8]) were the main mechanism of solidification cracking during SLM, we would expect solidification cracks in the modified alloy also. However, these specimens are entirely devoid of cracks. Since the SLM process parameters (such as laser power, laser scan speed, scanning strategy, substrate material, and substrate temperature) for standard and modified IN738LC were kept constant, it is a reasonable assumption that the spatial distribution of the thermal stresses, in the microstructure, during solidification is identical in both cases. Such minute modifications in Zr and Si content do not significantly alter the high-temperature yield stress and the ductility of the mushy zone. Hence, the suppression of the solidification crack formation in the modified alloy is primarily due to the reduction in the Zr and Si alloying content in the bulk composition. We, therefore, suggest that the increase of the solidification interval, due to the Zr enrichment, is not the dominant mechanism for solidification cracking of such nickel-base superalloys during the SLM process.

The modest influence of the solidification interval on solidification cracking is supported by earlier studies on casting and welding of nickel-base superalloys and Al alloys. Liu *et al.* [84] show that, although Al-4.0 Mg has a larger solidification interval as compared to Al-4.4 Cu, it has a lower cracking susceptibility during welding. Zhang and Singer [28] varied the Ti concentration in cast NBSs and reported that the alloy with the highest solidification interval had the least cracking susceptibility. The mechanism to initiate the hot tears in this alloy was attributed by Zhang and Singer to the increase in volume fraction of the liquid at the interdendritic region, influenced by Ti addition [28].

E. Concluding discussion

In summary, we have quantified the solute decoration to grain boundaries during the SLM process of IN738LC and discussed its influence on the solidification cracking mechanism. We have shown that (a) the composition profiles of B, C, and Zr, across GBs are affected by solid-state diffusion during cooling; (b) the mechanism of an increased critical temperature range (ΔT_{CTR}), due to solute enrichment of Zr is unsuited to explain the observed microcracking behavior; and (c) the model by Rappaz *et al.* [35] can account for the difference in cracking behavior seen on the HAGB and LAGB. However, the GB composition profile of minor solute species (Zr and Si) does not concur with the model predictions.

The basic argument by Rappaz *et al.* [35] for a higher crack susceptibility of the HAGB compared to the LAGB is that there exists an additional undercooling, required for full solidification. Hence, it could be described as a more sophisticated version of the simple ΔT_{CTR} model, which considers the effect of grain boundary energies (γ_{GB}) on the temperature range, and not only the difference between liquidus and solidus temperature. To accommodate the effect of a small change in minor solute elements in cracking susceptibility with this type of model, there needs to be a mechanism by which the minor element additions have a comparatively large influence on the undercooling (ΔT). We propose that the influence of, e.g., Zr and Si, is not via their effect on the bulk phase stability of the liquid and the solid phases, but rather on their effect on the grain boundary energies (γ_{GB}) and solid-liquid interface energies (γ_{SL}). The compositions of minor solute elements have additional contributions to the interface energies [85,86]. First-principles studies on the effect of solutes on grain boundary energies and on solid-state GB cohesion (quantified as "embrittling potency energy") have been reported. Embrittling potency energy is defined as the difference in the binding energy of a solute atom at a GB and a free surface [87]. Some studies describe a strengthening effect of Zr additions on the γ_{GB} of Ni [74], while other studies show a slight embrittling potency of Zr as well as an increase in γ_{GB} [87]. B, C, and Si reduce the embrittling potency energy by reducing the γ_{GB} in Ni [87,88]. Based on our experiments, we hypothesize that including the temperature and composition dependence of the interface energies into the undercooling model could lead to an understanding of the experimentally observed composition profiles. Extensive experimental and theoretical studies in Ni substantiate the influence of temperature and anisotropy on γ_{GB} and γ_{sl} [89–95].

The current paper clarifies that the enrichment of Si and Zr to the interdendritic liquid and its subsequent influence on the liquidus-solidus interval is not the dominant mechanism for solidification cracking in SLM-produced IN738LC. The cracking mechanism is most likely dominated by a combination of mechanical and chemical factors at several length scales. We are currently studying model nickel-base alloys with variations in minor solute element content (B, C, Zr, and Si) to unravel the solidification cracking mechanism during laser melting at a fundamental level. We are currently studying model nickel-base alloys with variations in minor solute element content (B, C, Zr, and Si) to unravel the solidification cracking mechanism during laser melting at a fundamental level. Previous studies have also shown that these minor solute species influence the cellular or dendritic type of growth during directional solidification of IN738 superalloy [96,97]. This improved understanding can be transferred to design a nickel-base superalloy, resistant to solidification cracking during the SLM process.

V. CONCLUSIONS

(1) During the selective laser melting process (SLM, also known as the laser powder bed fusion process) of polycrystalline nickel-base superalloy Inconel-738LC (IN738LC) the key issue is the presence of solidification cracks which typically nucleate in the semisolid intergranular region during the last stage of solidification and propagate along high angle grain boundaries only.

(2) Correlative atom probe tomography–transmission Kikuchi diffraction (APT-TKD) probing was capable of unambiguously distinguishing the misorientation-dependent enrichment profile of minor solute elements such as B, C, Zr, and Si in SLM-produced IN738LC. B and C enrich both the HAGBs and LAGBs. However, Zr and Si enrichment is only observed at HAGBs and not at LAGBs. These discrepancies demonstrate that the difference in the enrichment of minor solutes to HAGBs and LAGBs must be taken into account during the prediction of solute enrichment. This distinction cannot be made by simple Scheil-Gulliver calculations.

(3) APT-TKD analysis of GB chemistry at the topmost layer (a layer that experiences only a single laser pass) of the SLM produced a sample, showing similar enrichment profiles of solute elements, as compared to the GBs at the bottom layers. Hence the GB chemistry is not (significantly) influenced by the multiple “reheating” cycles, arising due to the melting and solidification of the subsequent top layers, during the SLM process.

(4) Microsegregation and solid-state segregation of solutes contribute to the final GB chemistry profiles. This difference in the GB enrichment mechanism is solute dependent. The GB profile of slow-diffusing solutes such as Si, Ti, and Nb is influenced by microsegregation only. However, solid-state segregation of fast-diffusing species such as B, C, and Zr during cooling after solidification could affect their respective enrichment profiles across the GB.

(5) A modified alloy composition of IN738LC with reduced Zr and Si content (wt. %), by 66 and 85%, respectively, was subjected to the SLM process. Postsolidification, microstructure analysis showed a 99% reduction in crack density, however with a comparable GB excess of Zr and Si quantified using APT. Hence, the current paper clarifies that the enrichment of Zr to the interdendritic liquid and its subsequent influence on the liquidus-solidus interval is not the dominant mechanism for solidification cracking in SLM-produced IN738LC.

(6) The misorientation-dependent GB solute enrichment profile from APT-TKD measurements was compared with the theory of misorientation-dependent coalescence of the remaining intergranular liquid by Rappaz *et al.* [35]. Zr and Si enrichment is more pronounced at HAGBs as compared to LAGBs. This experimental result is opposite to the predictions in the model. The inclusion of the temperature- and composition-dependent interface energies into the model may lead to an improved understanding of the experimentally observed composition profiles.

ACKNOWLEDGMENTS

A.H. gratefully acknowledges International Max Planck Research School for Interface Controlled Materials for Energy Conversion for a Ph.D. scholarship. Monika Nellessen and Katja Angenendt are acknowledged for their help with the EBSD data. Torsten Schwarz is acknowledged for the grain boundary excess calculations. The authors are grateful to Uwe Tezins and Andreas Sturm for their support at the APT and FIB facilities at MPIE.

[1] R. C. Reed, *The Superalloys: Fundamentals and Applications* (Cambridge University, Cambridge, England, 2008).
[2] G. Eggeler and A. Dlouhy, Acta Mater. **45**, 4251 (1997).
[3] T. M. Pollock and A. S. Argon, Acta Metall. Mater. **40**, 1 (1992).
[4] S. S. Babu, S. A. David, J. W. Park, and J. M. Vitek, Sci. Technol. Weld. Join. **9**, 1 (2004).
[5] R. K. Sidhu, O. A. Ojo, and M. C. Chaturvedi, Metall. Mater. Trans. A **38**, 858 (2007).
[6] A. T. Egbewande, H. R. Zhang, R. K. Sidhu, and O. A. Ojo, Metall. Mater. Trans. A **40**, 2694 (2009).
[7] M. M. Attallah, R. Jennings, X. Wang, and L. N. Carter, MRS Bull. **41**, 758 (2016).
[8] M. Cloots, P. J. Uggowitzer, and K. Wegener, Mater. Des. **89**, 770 (2016).
[9] N. J. Harrison, I. Todd, and K. Mumtaz, Acta Mater. **94**, 59 (2015).

[10] D. Tomus, P. A. Rometsch, M. Heilmaier, and X. Wu, Addit. Manuf. **16**, 65 (2017).
[11] J. Campbell, *Castings*, 2nd ed. (Butterworth-Heinemann, Burlington, MA, 2003).
[12] S. Kou, *Welding Metallurgy*, 2nd ed. (Wiley, New York, 2003).
[13] I. Farup, J.-M. Drezet, and M. Rappaz, Acta Mater. **49**, 1261 (2001).
[14] J. Lippold, S. D. Kiser, and J. N. DuPont, *Welding Metallurgy and Weldability of Nickel-Base Alloys* (Wiley, New York, 2011).
[15] *Hot Cracking Phenomena in Welds II*, edited by T. Böllinghaus, H. Herold, C. E. Cross, and J. C. Lippold (Springer-Verlag, Berlin, 2008).
[16] O. A. Ojo, N. L. Richards, and M. C. Chaturvedi, Scr. Mater. **51**, 683 (2004).
[17] O. A. Ojo, N. L. Richards, and M. C. Chaturvedi, Mater. Sci. Technol. **20**, 1027 (2004).
[18] O. A. Idowu, O. A. Ojo, and M. C. Chaturvedi, Metall. Mater. Trans. A **37**, 2787 (2006).
[19] M. Zhong, H. Sun, W. Liu, X. Zhu, and J. He, Scr. Mater. **53**, 159 (2005).
[20] M. Abdelfatah and O. A. Ojo, Mater. Sci. Technol. **25**, 61 (2009).
[21] L. Rickenbacher, T. Etter, S. Hövel, and K. Wegener, Rapid Prototyp. J. **19**, 282 (2013).
[22] M. Cloots, K. Kunze, P. J. Uggowitzer, and K. Wegener, Mater. Sci. Eng. A **658**, 68 (2016).
[23] D. G. Eskin and L. Katgerman, Metall. Mater. Trans. A **38**, 1511 (2007).
[24] N. Coniglio and C. E. Cross, Int. Mater. Rev. **58**, 375 (2013).
[25] K. C. Anthony and J. F. Radavich, *Superalloys 1976*, Third International Symposium, TMS (1976), p. 137.
[26] J. N. Dupont, J. Mater. Sci. **32**, 4101 (1997).
[27] K. Heck, R. Blackford, and R. F. Singer, Mater. Sci. Technol. **15**, 213 (1999).
[28] J. Zhang and R. F. Singer, Acta Mater. **50**, 1869 (2002).
[29] J. Zhang and R. F. Singer, Metall. Mater. Trans. A **35**, 1337 (2004).
[30] J. Zhang and R. F. Singer, Metall. Mater. Trans. A **35**, 939 (2004).
[31] M. Rappaz, J.-M. Drezet, and M. Gremaud, Metall. Mater. Trans. A **30**, 449 (1999).
[32] L. Wang, N. Wang, and N. Provatas, Acta Mater. **126**, 302 (2017).
[33] J. A. Dantzig and M. Rappaz, *Solidification* (EPFL, Lausanne, 2016).
[34] N. Wang, S. Mokadem, M. Rappaz, and W. Kurz, Acta Mater. **52**, 3173 (2004).
[35] M. Rappaz, A. Jacot, and W. J. Boettinger, Metall. Mater. Trans. A **34**, 467 (2003).
[36] W. Kurz and D. J. Fisher, *Fundamentals of Solidification* (Trans Tech, Lausanne, 1986).
[37] R. Engeli, T. Etter, S. Hövel, and K. Wegener, J. Mater. Process. Technol. **229**, 484 (2016).
[38] R. T. Holt and W. Wallace, Int. Mater. Rev. **21**, 1 (1976).
[39] Y. Zhu, S. Zhang, T. Zhang, J. Zhang, Z. Hu, X. Xie, and C. Shi, *Superalloys 1992*, Seventh International Symposium, TMS (1992).
[40] B. Geddes, H. Leon, and X. Huang, *Superalloys: Alloying and Performance* (ASM International, Ohio, 2010).
[41] T. J. Kelly, Weld. J. **68**, 44s (1989).
[42] D. W. Brown, J. D. Bernardin, J. S. Carpenter, B. Clausen, D. Spernjak, and J. M. Thompson, Mater. Sci. Eng. A **678**, 291 (2016).
[43] O. Fergani, F. Berto, T. Welo, and S. Y. Liang, Fatigue Fract. Eng. Mater. Struct. **40**, 971 (2017).
[44] K. An, L. Yuan, L. Dial, I. Spinelli, A. D. Stoica, and Y. Gao, Mater. Des. **135**, 122 (2017).
[45] T. Mukherjee, J. S. Zuback, W. Zhang, and T. Debroy, Comput. Mater. Sci. **143**, 325 (2018).
[46] W. J. Sames, F. A. List, S. Pannala, R. R. Dehoff, and S. S. Babu, Int. Mater. Rev. **61**, 315 (2016).
[47] M. M. Nowell and S. I. Wright, Ultramicroscopy **103**, 41 (2005).
[48] K. Thompson, D. Lawrence, D. J. Larson, J. D. Olson, T. F. Kelly, and B. Gorman, Ultramicroscopy **107**, 131 (2007).
[49] R. R. Keller and R. H. Geiss, J. Microsc. **245**, 245 (2012).
[50] A. J. Breen, K. Babinsky, A. C. Day, K. Eder, C. J. Oakman, P. W. Trimby, S. Primig, J. M. Cairney, and S. P. Ringer, Microsc. Microanal. **23**, 279 (2017).
[51] T. F. Kelly and M. K. Miller, Rev. Sci. Instrum. **78**, 031101 (2007).
[52] F. Vurpillot, A. Cerezo, D. Blavette, and D. J. Larson, Microsc. Microanal. Off. J. Microsc. Soc. Am. Microbeam Anal. Soc. Microsc. Soc. Can. **10**, 384 (2004).
[53] T. Schwarz, G. Stechmann, B. Gault, O. Cojocaru-Mirédin, R. Wuerz, and D. Raabe, Prog. Photovolt. Res. Appl. **26**, 196 (2018).
[54] B. W. Krakauer and D. N. Seidman, Phys. Rev. B **48**, 6724 (1993).
[55] K. Kunze, T. Etter, J. Grässlin, and V. Shklover, Mater. Sci. Eng. A **620**, 213 (2015).
[56] T. Vilaro, C. Colin, J. D. Bartout, L. Nazé, and M. Sennour, Mater. Sci. Eng. A **534**, 446 (2012).
[57] E. A. Jägle, Z. Sheng, L. Wu, L. Lu, J. Risse, A. Weisheit, and D. Raabe, JOM **68**, 943 (2016).
[58] D. Gu, Y.-C. Hagedorn, W. Meiners, G. Meng, R. J. S. Batista, K. Wissenbach, and R. Poprawe, Acta Mater. **60**, 3849 (2012).
[59] M. Das, V. K. Balla, D. Basu, S. Bose, and A. Bandyopadhyay, Scr. Mater. **63**, 438 (2010).
[60] D. G. Brandon, Acta Metall. **14**, 1479 (1966).
[61] D. Raabe, M. Herbig, S. Sandlöbes, Y. Li, D. Tytko, M. Kuzmina, D. Ponge, and P.-P. Choi, Curr. Opin. Solid State Mater. Sci. **18**, 253 (2014).
[62] D. Tytko, P.-P. Choi, J. Klöwer, A. Kostka, G. Inden, and D. Raabe, Acta Mater. **60**, 1731 (2012).
[63] S. Kou, JOM **55**, 37 (2003).
[64] T. F. Bower, H. D. Brody, and M. C. Flemings, Trans. Metall. Soc. AIME **236**, 624 (1966).
[65] H. D. Brody, *Solute Redistribution in Dendritic Solidification* (MIT, Cambridge, MA, 1965).
[66] T. W. Clyne and W. Kurz, Metall. Trans. A **12**, 965 (1981).
[67] S. Kobayashi, J. Cryst. Growth **88**, 87 (1988).
[68] I. Ohnaka, Trans. Iron Steel Inst. Jpn. **26**, 1045 (1986).
[69] W. Kurz, B. Giovanola, and R. Trivedi, Acta Metall. **34**, 823 (1986).
[70] B. Giovanola and W. Kurz, Metall. Trans. A **21**, 260 (1990).
[71] S. C. Flood and J. D. Hunt, Appl. Sci. Res. **44**, 27 (1987).
[72] M. H. Burden and J. D. Hunt, J. Cryst. Growth **22**, 109 (1974).
[73] C. Y. Wang and C. Beckermann, Metall. Mater. Trans. A **25**, 1081 (1994).

[74] P. Lejček, M. Šob, and V. Paidar, Prog. Mater. Sci. **87**, 83 (2017).

[75] E. D. Hondros and M. P. Seah, Int. Met. Rev. **22**, 262 (1977).

[76] J. E. Ramirez and S. Liu, Weld. J. **71**, 365 (1992).

[77] C. Z. Hargather, S.-L. Shang, and Z.-K. Liu, Acta Mater. **157**, 126 (2018).

[78] C. Z. Hargather, S.-L. Shang, and Z.-K. Liu, Data Brief **20**, 1537 (2018).

[79] See Supplemental Material at http://link.aps.org/supplemental/10.1103/PhysRevMaterials.3.123602 for the diffusion coefficients of all the solutes.

[80] See Supplemental Material at http://link.aps.org/supplemental/10.1103/PhysRevMaterials.3.123602 for the APT analysis.

[81] J. N. DuPont, M. R. Notis, A. R. Marder, C. V. Robino, and J. R. Michael, Metall. Mater. Trans. A **29**, 2785 (1998).

[82] A. K. Jena and M. C. Chaturvedi, J. Mater. Sci. **19**, 3121 (1984).

[83] E. Chauvet, P. Kontis, E. A. Jägle, B. Gault, D. Raabe, C. Tassin, J.-J. Blandin, R. Dendievel, B. Vayre, S. Abed, and G. Martin, Acta Mater. **142**, 82 (2018).

[84] J. Liu, H. P. Duarte, and S. Kou, Acta Mater. **122**, 47 (2017).

[85] W. D. Kingery, J. Am. Ceram. Soc. **37**, 42 (1954).

[86] T. Cheng, D. Fang, and Y. Yang, J. Appl. Phys. **123**, 085902 (2018).

[87] M. Yamaguchi, M. Shiga, and H. Kaburaki, J. Phys. Condens. Matter **16**, 3933 (2004).

[88] V. I. Razumovskiy, A. Y. Lozovoi, and I. M. Razumovskii, Acta Mater. **82**, 369 (2015).

[89] W. R. Tyson and W. A. Miller, Surf. Sci. **62**, 267 (1977).

[90] T. A. Roth, Mater. Sci. Eng. **18**, 183 (1975).

[91] J. J. Hoyt, M. Asta, and A. Karma, Phys. Rev. Lett. **86**, 5530 (2001).

[92] B. B. Laird, R. L. Davidchack, Y. Yang, and M. Asta, J. Chem. Phys. **131**, 114110 (2009).

[93] H. M. Lu, Z. Wen, and Q. Jiang, Colloids Surf. Physicochem. Eng. Asp. **278**, 160 (2006).

[94] Y. Yang, M. Asta, and B. B. Laird, Phys. Rev. Lett. **110**, 096102 (2013).

[95] S. I. Prokofjev, J. Mater. Sci. **52**, 4265 (2017).

[96] H. Zhu, Y. Tang, Y. Li, Y. Zhu, Z. Hu, and C. Shi, Mater. High Temp. **10**, 39 (1992).

[97] H. Q. Zhu, S. R. Guo, H. R. Guan, V. X. Zhu, Z. Q. Hu, V. Murata, and M. Morinaga, Mater. High Temp. **12**, 285 (1994).